

Three-Dimensional Mathematical Model of Oxygen Transport Behavior in Electroslag Remelting Process



XUECHI HUANG, BAOKUAN LI, and ZHONGQIU LIU

A transient three-dimensional model has been proposed to investigate the oxygen transport behavior in electroslag remelting process. The electromagnetism, heat transfer, multiphase flow, and species transport were calculated simultaneously by finite volume method. The volume of fluid approach was adopted to trace the metal–slag–air three-phase flow. Based on the necessary thermodynamics of oxygen transport behavior, a kinetic model was established to predict the mass source terms in species transport equation. The kinetic correction factor was proposed to account for the effect of the oxide scale formed on the electrode on the FeO content in slag. Finally, the effect of applied current on the oxygen transfer was studied. The predicted result agrees well with the measured data when the kinetic correction factor is set to be 0.5. The temperature distribution that affects the thermodynamics differs at the interfaces. The oxygen in air is absorbed into slag due to the oxidation at the slag/air interface. The Fe₂O₃ in slag and the oxide scale contribute to the increase of FeO content in slag, and the latter one plays the leading role. The oxygen transfer from slag to metal mainly occurs during the formation of the droplet at the slag/metal droplet interface. With the current increasing from 1200 to 1800 A, the oxygen content increases from 76.4 to 89.8 ppm, and then slightly declines to 89.2 ppm when the current increases to 2100 A.

<https://doi.org/10.1007/s11663-017-1158-7>

© The Minerals, Metals & Materials Society and ASM International 2017

I. INTRODUCTION

ELECTROSLAG remelting (ESR) is widely employed for producing high performance steels and nickel-based alloys due to its unique advantages, such as the effective control of steel chemistry, excellent solidification structure and surface quality of final ingots, and powerful removal of non-metallic inclusions.^[1,2] During this process, a direct or alternating current (DC/AC) is applied in the system, and the Joule heating in the slag is sufficient to melt the electrode. The molten metal feeds a liquid metal pool, which solidified directionally in the water-cooled mold. It is generally known that oxygen in steel, which will cause unwanted pores and generation of oxide inclusions during solidification, influences the steel quality.^[3,4] Its removal has been a tough task for many metallurgists for a long time. The initial oxygen in the electrode, the oxygen in the atmosphere, the oxide scale formed on the electrode, and the slag composition affect the oxygen transport behavior as well as the oxygen

content in ESR ingot. Besides, the mass transfer process and species distribution are influenced by the multi-physical fields, especially the temperature distribution and the flow field. Therefore, it is essential to have a further and comprehensive understanding of oxygen transport behavior in ESR process.

Lots of experimental investigations on the oxygen transfer have been done in the past decades.^[3,5–8] Researchers confirmed that the ferrous oxide (FeO) content at the slag/metal interface, which represents the oxygen potential of slag, affects the oxygen transport behavior dramatically. However, the information provided by experiments was limited. The interaction among the multi-physical fields, especially the effect of temperature distribution and flow field on the mass transfer process was difficult to analyze. In this case, numerical simulation is widely adopted to perform fundamental studies owing to its low cost, simple implementation, and visualization. Weber *et al.*^[9] developed a transient model to account for electromagnetic phenomena as well as heat and momentum transfer in an axisymmetrical geometry. The melt pool profile was predicted accurately. Kharicha *et al.*^[10] numerically investigated the interaction between the electro-dynamics and the phase distribution in ESR process. The interface tension and current frequency significantly affected the droplet formation. But their work ignored the mass transfer in ESR process. Recently, Wang *et al.*^[11,12] first

XUECHI HUANG, BAOKUAN LI, and ZHONGQIU LIU are with the School of metallurgy, Northeastern University, Shenyang 110819, People's Republic of China. Contact e-mail: libk@smm.neu.edu.cn

Manuscript submitted July 19, 2017.

Article published online December 19, 2017.

established a comprehensive model to numerically describe the desulfurization and oxygen transfer during the direct current (DC) ESR process. The electrochemical reaction, which plays a major role in DC system, was carefully considered. However, the interaction among the slag and metal compositions were not taken into account.

As mentioned above, the attempts to numerically investigate the oxygen transport behavior in AC ESR process was still insufficient. And it is not clear that if the oxide scale or the Fe_2O_3 takes a leading role affecting the increase of FeO content in slag. In the present work, the authors aimed to establish a three-dimensional mathematical model to have a basic understanding of oxygen transport behavior among slag, metal, and air. In this process, the flow field influences the species distribution, while the temperature field determines the thermodynamics. Therefore, the electromagnetism, three-phase flow, heat transfer, and species transport were simultaneously calculated. The oxygen transport behavior was predicted by a kinetic model based on the necessary thermodynamics. A kinetic correction factor was proposed to account for the effect of the oxide scale formed on the electrode on the FeO content in slag. An experiment was implemented to validate and correct the model. Furthermore, the effect of applied current on the oxygen transport behavior was also investigated.

II. MODEL DESCRIPTION

A. Assumptions

The mathematical model for the oxygen transport behavior coupled with electromagnetism, three-phase flow, heat transfer, and species transport is based on the following assumptions:

1. The computational domain includes the molten slag, the liquid metal pool, and the air. The water-cooled mold is not taken into account, and the mold lateral wall is assumed to be non-conductive electrically.^[13]
2. The solidification and volatilization are ignored.
3. The properties of each phase including density and electrical conductivity are temperature dependent, and the others were supposed to be constant.^[14]
4. The oxygen partial pressure in the air phase remains constant.
5. The desired elements include oxygen, iron, silicon, manganese, and aluminum, while the others are neglected.

B. VOF Approach

The VOF approach is adopted to trace the interfaces among slag, metal, and air^[15]:

$$\frac{\partial \alpha_i}{\partial t} + \nabla \cdot (\vec{v} \alpha_i) = 0, \quad [1]$$

where α_i represents the volume fraction of the metal, slag, and air, respectively. Thus, the properties of the mixture phase can be expressed as:

$$\bar{\phi} = \phi_m \alpha_m + \phi_s \alpha_s + \phi_g \alpha_g \quad [2]$$

C. Electromagnetic Field

The electromagnetic field created by an alternative current is described by Maxwell's equations. The electric potential method is used to solve the electromagnetic field.^[16] The electric field intensity can be written as the gradient of electric potential, while the magnetic potential vector is introduced to solve the magnetic field. As a consequence, the Joule heating and electromagnetic force are calculated, and incorporated into energy and momentum conservation equations, respectively:

$$Q_J = \frac{\vec{J} \cdot \vec{J}}{\bar{\sigma}}, \vec{F}_e = \vec{J} \times \vec{B} \quad [3]$$

D. Fluid Flow and Heat Transfer

The flow field is modeled by the continuity equation and Navier–Stokes equation^[17]:

$$\frac{\partial \rho}{\partial t} + \nabla \cdot (\rho \vec{v}) = 0 \quad [4]$$

$$\frac{\partial(\rho \vec{v})}{\partial t} + \nabla \cdot (\rho \vec{v} \otimes \vec{v}) = -\nabla p + \mu_{eff} \nabla^2 \vec{v} + \rho \vec{g} + \vec{F}_e + \vec{F}_b + \vec{F}_{st}, \quad [5]$$

where \vec{F}_b is the buoyancy force calculated by Boussinesq approximation. \vec{F}_{st} is the surface tension. μ_{eff} represents the effective viscosity composed of the laminar and turbulent viscosities, and the RNG $k-\varepsilon$ turbulence model is used to calculate the turbulent one.^[12]

The temperature distribution is described precisely by the energy conservation equation^[18]:

$$\frac{\partial}{\partial t}(\rho E) + \nabla \cdot (\vec{v} \rho E) = \nabla \cdot (k_{eff} \nabla T) + Q_J, \quad [6]$$

where k_{eff} is the effective thermal conductivity, $k_{eff} = bc_p \mu_{eff}$ (where b is inverse Prandtl number). The internal energy of the mixture phase E is associated with the specific heat and temperature:

$$E = \frac{\alpha_m \rho_m c_{p,m} + \alpha_s \rho_s c_{p,s} + \alpha_g \rho_g c_{p,g}}{\alpha_m \rho_m + \alpha_s \rho_s + \alpha_g \rho_g} T \quad [7]$$

E. Mass Transfer

The mass transfer in AC ESR process depends on the chemical reactions among slag, metal, and air. The species distribution is determined by the molecular diffusion as well as the turbulent flow. The process can be represented by^[19]:

$$\frac{\partial(\rho c)}{\partial t} + \nabla \cdot (\rho \vec{v} c) = \nabla \cdot (D_{eff,i} \nabla c) + S_i, \quad [8]$$

where c is the mass fraction. $D_{eff,i}$ is the effective diffusion coefficient. The turbulent diffusion coefficient can be calculated by $D_{t,i} = \frac{\mu_i}{\rho S c_i}$. S_i is mass source term in species transport equation due to chemical reactions at the interfaces.

1. At slag/metal interface

The diffusion rate is generally supposed to be the restrictive step of the mass transfer process rather than the chemical reaction rate. It is hard to separate the individual effects of mass transfer in both phases experimentally. Hence, an overall mass transfer coefficient is adopted in the present work, and the source terms can be expressed as^[20]:

$$S_i = -\rho_m k_{T,i} A \left(w[i] - \frac{w(i)}{L_i} \right), \quad [9]$$

where $w[i]$, $w(i)$ are the mass fraction of species i in metal and slag, respectively. A is the specific surface area.^[21] L_i is the equilibrium distribution ratio at the interfaces:

$$L_i = \frac{w(i)^*}{w[i]^*}, \quad [10]$$

where $w[i]^*$ and $w(i)^*$ represent the equilibrium content of species in metal and slag at slag/metal interface, respectively.

The overall mass transfer coefficient is given by:

$$k_{T,i} = \frac{1}{\left(\frac{1}{k_{m,i}} + \frac{\rho_m}{k_{s,i} L_i \rho_s} \right)}, \quad [11]$$

where $k_{m,i}$, $k_{s,i}$ are the mass transfer coefficient of species i in metal and slag, respectively. The mass transfer coefficient can be deduced by the diffusion coefficient^[22]:

$$k_{m,i} \propto D_{m,i}^{0.5} \left(\frac{\varepsilon}{v_m} \right)^{0.25}, \quad k_{s,i} \propto D_{s,i}^{0.5} \left(\frac{\varepsilon}{v_s} \right)^{0.25} \quad [12]$$

2. At slag/air interface

At the slag/air interface, the source terms in slag and air are expressed as follows, respectively^[23]:

$$S_i = -\rho_s k_{s,i} A (w(i) - w(i)^*) \quad [13]$$

$$S_i = -M_i \frac{k_{g,i}}{RT} A (P_i - P_i^*), \quad [14]$$

where P_i is partial pressure at the slag/air interface. $k_{g,i}$ is the mass transfer coefficient in air.

F. Kinetic Model

Based on the thermodynamics, a kinetic model is proposed to predict the mass source terms. The chemical reaction sites can be summarized as follows: the slag/metal interface (including the slag/metal droplet interface and the slag/metal pool interface) and the slag/air

interface. The schematic illustration of oxygen transport behavior in ESR process is shown in Figure 1.

1. At slag/metal interface

The FeO activity dominates the oxygen potential of the slag phase, and also influences the oxygen transport behavior at the slag/metal interface. The change of FeO content results from the oxidation of air, the melt of oxide scale generated on the electrode surface before and during the ESR process, and the loss of the active elements such as silicon and manganese. Therefore, the mechanism of oxygen transport behavior involving [Fe], [Si], [Mn], and [Al] can be expressed by^[24]:

$$[Fe] + [O] = (FeO) \log K_{FeO} = \frac{6150}{T} - 2.604 = \log \frac{a_{FeO}}{a_{Fe} \cdot a_O}, \quad [15]$$

$$\begin{aligned} [Si] + 2(FeO) &= (SiO_2) + [Fe] \log K_{Si} = \frac{17770}{T} - 6.122 \\ &= \log \frac{a_{SiO_2} a_{Fe}^2}{a_{Si} \cdot a_{FeO}^2}, \end{aligned} \quad [16]$$

$$\begin{aligned} [Mn] + (FeO) &= (MnO) + [Fe] \log K_{Mn} \\ &= \frac{8695}{T} - 3.93 = \log \frac{a_{MnO} a_{Fe}}{a_{Mn} \cdot a_{FeO}}, \end{aligned} \quad [17]$$

$$\begin{aligned} 2[Al] + 3(FeO) &= (Al_2O_3) + 3[Fe] \log K_{Al} \\ &= \frac{45130}{T} - 12.208 = \log \frac{a_{Al_2O_3} a_{Fe}^3}{a_{Al}^2 \cdot a_{FeO}^3}, \end{aligned} \quad [18]$$

$$\begin{aligned} (Fe_2O_3) + [Fe] &= 3(FeO) \log K_{Fe_2O_3} \\ &= -0.00283T + 11.9 - \frac{6909}{T} = \log \frac{a_{FeO}^3}{a_{Fe_2O_3} \cdot a_{Fe}}, \end{aligned} \quad [19]$$

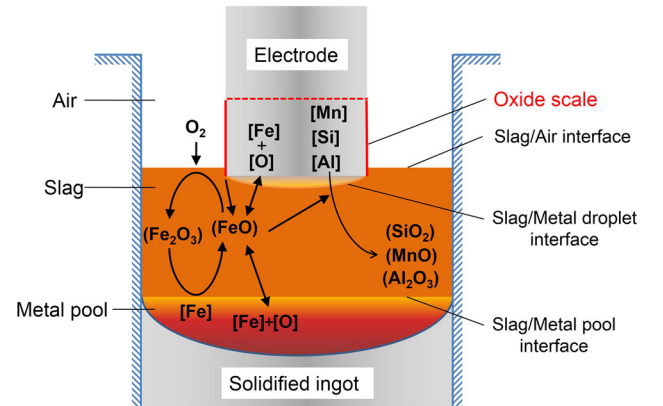


Fig. 1—Schematic of oxygen transport behavior in ESR process.

where a_i is the activity of species i in metal and slag. The activities of the components in metal are estimated by Henry's law:

$$a_i = f_i w[i], \log f_i = \sum e'_i w'[i], \quad [20]$$

where f_i is the Henry activity coefficient. e'_i is the interaction coefficients between the elements in metal.

On the other side, the activities of the oxides in slag can be calculated by Raoult's law:

$$a_i = \gamma_i X_i \quad [21]$$

where X_i represents the molar fraction of the oxide in slag. γ_i is the Raoult activity coefficient, and can be deduced according to Reference 25.

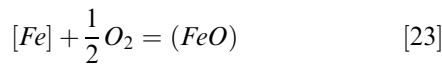
Combining Eqs. [15] through [21], the interfacial distribution ratios can be expressed by the thermodynamic equilibrium constants, activity coefficients, and interfacial activity of oxygen. Then, the mass source terms can be written in the form of Eq. [9].

In addition, a mass balance equation of FeO at the slag/metal interface was applied to calculate the only unknown parameter, *i.e.*, interfacial activity of oxygen, in order to close the kinetic model:

$$2 \frac{S_{Si}}{M_{Si}} + \frac{S_{Mn}}{M_{Mn}} + 1.5 \frac{S_{Al}}{M_{Al}} + \frac{S_O}{M_O} = \frac{S_{FeO,Slag}}{M_{FeO}} + 3 \frac{S_{Fe_2O_3}}{M_{Fe_2O_3}}, \quad [22]$$

where M_i is the molecular weight. $S_{FeO,Slag}$ represents the mass source term of FeO at the slag/metal interface caused by slag composition. The left side of Eq. [22] represents the consumption of FeO at the slag/metal interface, and the right side the supply.

Despite the oxide scale formed on the electrode was meticulously cleaned up in advance, the oxide scale regenerated during the ESR process could not be neglected. Unfortunately, it is difficult to accurately predict its effect on the FeO content in slag. In this case, we make the following assumptions for a simple model: (1) The ingredient of the oxide scale is FeO under high temperature condition. (2) The oxide scale is completely melted into the slag phase at the slag/metal interface very close to the electrode tip. As a result, the corresponding oxidation reaction as well as the mass source term can be expressed according to Arrhenius equation^[26]:



$$S_{FeO,Oxide\ scale} = \begin{cases} -C_k \exp(A_0 - \frac{Q}{RT}) & \text{the slag/metal interface, } Z ; 130 \text{ mm} \\ 0 & \text{else} \end{cases} \quad [24]$$

where C_k is the kinetic correction factor proposed to fit the calculated FeO content to experimental one. Q is the activation energy. A_0 is the model constant.

The overall mass source term of FeO consists of two parts calculated above:

$$S_{FeO} = S_{FeO,Slag} + S_{FeO,Oxidescale} \quad [25]$$

2. At slag/air interface

During the conventional ESR process, the molten slag is exposed in the open atmosphere. The FeO will be oxidized by the oxygen in air, which causes the increase of Fe₂O₃ content^[27]:

$$\begin{aligned} 2(FeO) + \frac{1}{2} O_2 &= (Fe_2O_3) \log K_{O_2} \\ &= \frac{3166.6}{T} - 1.324 = \log \frac{a_{Fe_2O_3}}{a_{FeO}^2 \cdot P_{O_2}^{0.5}} \end{aligned} \quad [26]$$

The solution method is the same as above. The necessary mass balance equation of oxygen at the slag/air interface is given by:

$$\frac{S_{FeO}}{M_{FeO}} + 3 \frac{S_{Fe_2O_3}}{M_{Fe_2O_3}} = 2 \frac{S_{O_2}}{M_{O_2}} \quad [27]$$

G. Boundary Conditions

The boundary conditions of the current model are shown in Figure 2.^[28] A potential gradient is imposed at the slag/electrode tip interface in order to account for the skin effect.^[29] According to the insulation hypothesis of the mold, the potential gradient at the mold lateral wall is supposed to be zero. Meanwhile, a melting rate at the electrode tip is written as a function of the Joule heating^[11]:

$$\dot{m} = \frac{\eta Q_J}{A_{electrode} L}, \quad [28]$$

where η represents the power efficiency according to experiments and literature. L is the latent heat of fusion of metal.

Accordingly, a mass flow inlet boundary with nominal content of electrode is adopted at the electrode tip. The air top surface is set to be outflow boundary, while the mold wall and the electrode side are supposed to be non-slipping wall boundaries. The bottom is assumed to be velocity inlet boundary with a negative axial velocity. The negative velocity is deduced according to the melting rate of electrode. The temperature at the electrode tip has a 20 K superheat than the liquidus of metal.^[30] It must be noticed that the diffusion coefficients of components in each phase vary a lot in different literatures, and are specified as averaged values for simplification.^[23,31-33] The detailed parameters are listed in Table I.^[17,34-37]

III. NUMERICAL PROCEDURE

In the present work, the CFD software Fluent 12.0 with user-defined functions (UDFs) was used to solve the coupled mathematical model based on the finite

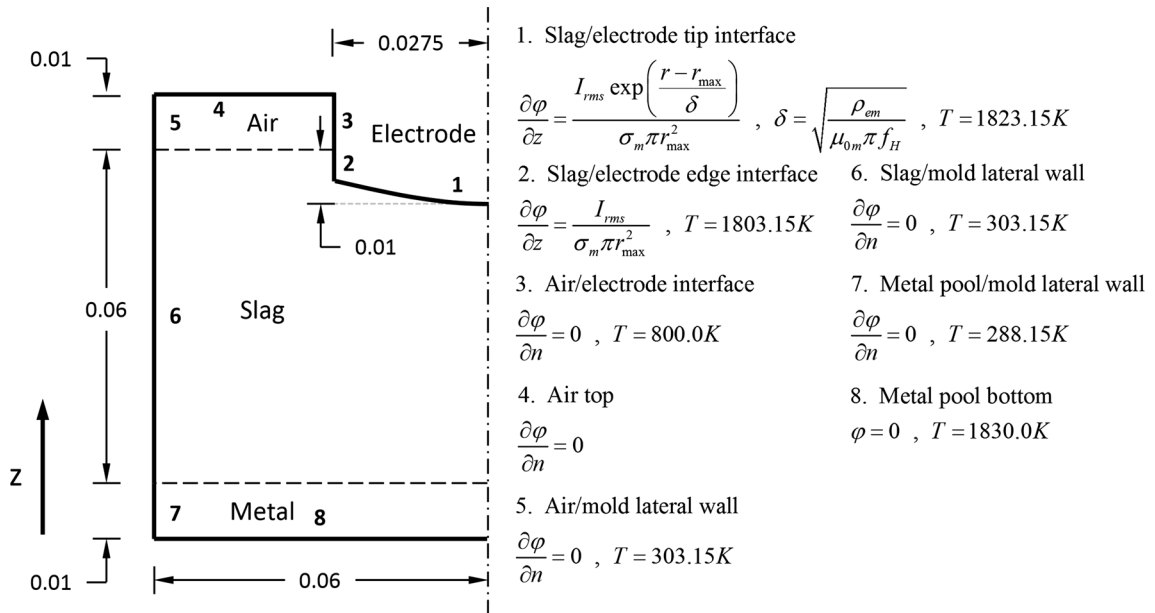


Fig. 2—Boundary conditions and dimensions of ESR model in this study.

Table I. Physical Properties and Operation Conditions Used in this Study

Physical Properties	Value		
	Metal	Slag	Air
Density (kg/m ³)	7500	2800	1.29
Viscosity (Pa·s)	0.0061	0.025	1.79 × 10 ⁻⁵
Specific heat (J/kg·K)	752	1250	1006.43
Thermal conductivity (W/m·K)	30.5	10.5	0.0242
Diffusion coefficient of elements (m ² /s)	6.25 × 10 ⁻⁹	4.0 × 10 ⁻⁹	1.59 × 10 ⁻⁴
Electric conductivity (1/(Ω·m))	7.14 × 10 ⁵	ln σ = -6769/T + 8.818	—
Magnetic permeability (H/m)	4π × 10 ⁻⁷	4π × 10 ⁻⁷	—
Liquidus temperature (K)	1803.15	—	—
Thermal expansion coefficient (1/K)	2 × 10 ⁻⁴	4 × 10 ⁻⁴	—
Operating condition			
Current (A)	1200/1500/1800/2100		
Frequency (Hz)	50		

volume method. Figure 3 shows the solution schematic of the current model. Phase distributions of slag, metal, and air were updated at each iteration. The magneto-hydrodynamic (MHD) module was loaded as UDFs to describe the electromagnetic phenomenon. The electromagnetic force and the Joule heating were incorporated into the momentum and energy conservation equations, respectively. On the basis of the distributions of temperature and species at the interfaces the mass source terms were calculated, and invoked into the species transport equations as UDFs. Then the multi-physical fields could be solved simultaneously. In addition, the whole domain was divided into 739240 structured grids as shown in Figure 4, and an extremely refined mesh was imposed at the interfaces in order to improve the accuracy. The time step size was set to be 0.001 second to meet the convergence criteria (10⁻⁶).

IV. RESULTS AND DISCUSSION

A. Experimental Details and Model Validation

A laboratory experiment under the atmosphere condition was implemented to validate and correct this model. The 60 kg scale ESR furnace was used as displayed in Figure 5. The inner diameter and height of mold are 120 and 600 mm, respectively. The original composition of the consumable electrode was (wt pct): C 0.052, Mn 1.28, Si 0.41, Ni 8.85, Cr 17.78, Al 0.0014, O 0.0056. The original slag was (wt pct): CaF₂ 69.9, Al₂O₃ 29.9, FeO 0.2. An alternative current (1500 A) flowed in at the electrode and out at the baseplate. The whole ESR process lasted about 30 minutes, and no deoxidation treatment was performed during this process. The slag temperature was measured by disposable W3Re/W25Re thermocouples. The slag and metal samples were also

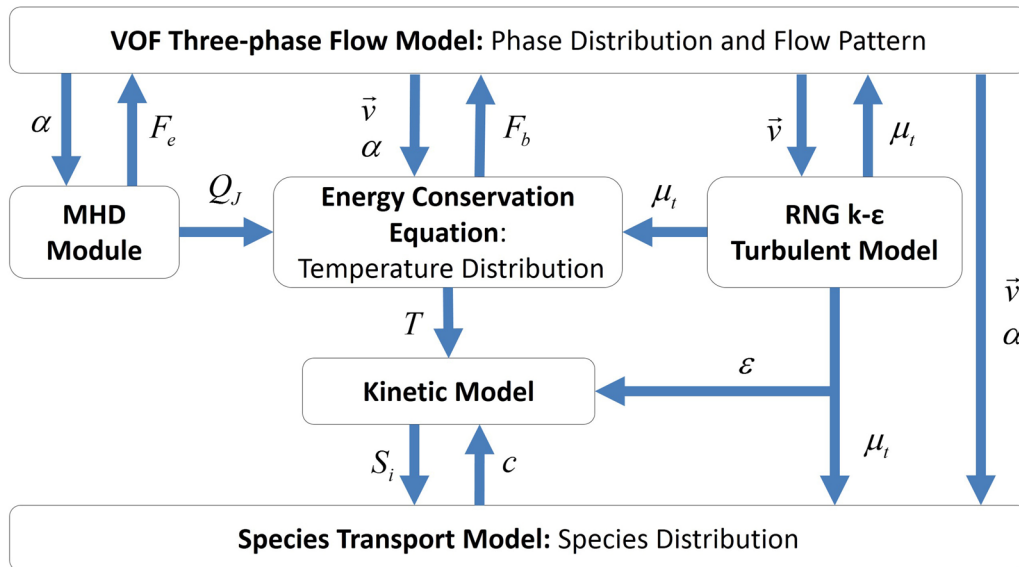


Fig. 3—Solution schematic of the current model.

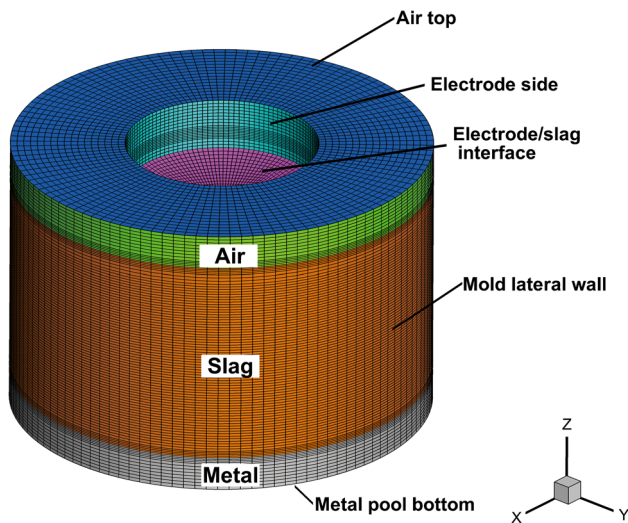


Fig. 4—Mesh model.

extracted by a spring and a quartz glass tube during the ESR process, respectively. The nitrogen/oxygen analyzer was employed to determine the oxygen content in the samples of metal. The FeO content in slag was detected by the potassium dichromate volumetric method in the atmosphere of carbon dioxide. The other elements were detected by the optical direct-reading spectrometer.

Figure 6 displays the comparison of temperature in the slag layer between calculated and measured results. The calculated data rises with height in the slag layer, and shows a sharp drop in the air layer. The simulated and measured results are in good agreement with an acceptable error. The discrepancy mainly results from the uncertainty of material properties and boundary conditions, the electrical insulation hypothesis of the mold and the measuring errors.



Fig. 5—Photo of the laboratory experiment.

In this model, the kinetic correction factor C_k is proposed to consider the effect of oxide scale on the change of FeO content in slag. The simulated evolution of FeO content in slag with different values of C_k is shown in Figure 7. It can be observed that FeO content increases over time. Particularly, the growth rate of FeO content declines at the later stage owing to the increasing loss of active elements in metal. With the increase of C_k , FeO content becomes higher. When the kinetic correction factor is 0.5, the calculated and measured results agree well with each other.

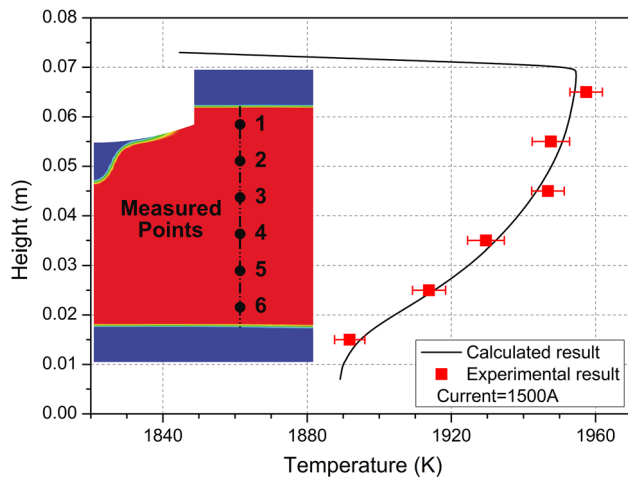


Fig. 6—Comparison of temperature in the slag layer between the simulation and experiment.

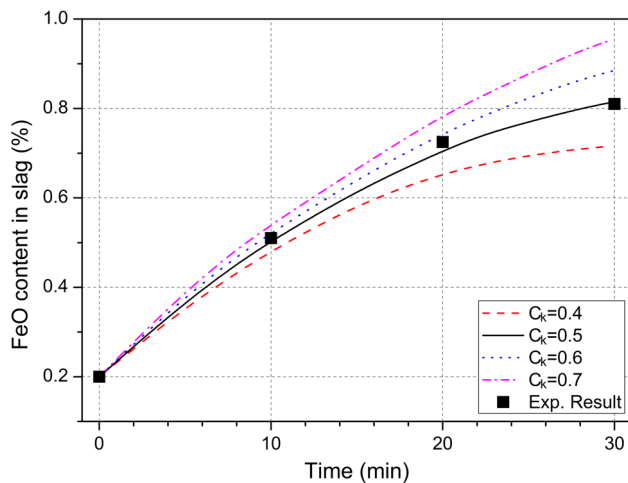


Fig. 7—Comparison of FeO content in slag between the simulation and experiment.

The comparison of oxygen content in the metal pool between the simulated and measured data is demonstrated in Figure 8. The kinetic correction factor is set to be 0.5. Since there was no deoxidizer added during the ESR process, the FeO content in slag directly influences the change of oxygen content in the metal pool. We can see that the oxygen content in metal rises with time. The oxygen is removed from the metal at the initial stage when the FeO content is relatively low, and is abstracted into the metal for the rest of the time. The good agreement between the simulation and experiment indicates that the current model is able to give a further prediction of the oxygen transport behavior in ESR process.

B. MHD Fluid Flow and Temperature Distribution

Figure 9 demonstrates the slag phase distribution at 1329.35 seconds. It can be seen that the molten metal converges to the center of the electrode tip under the

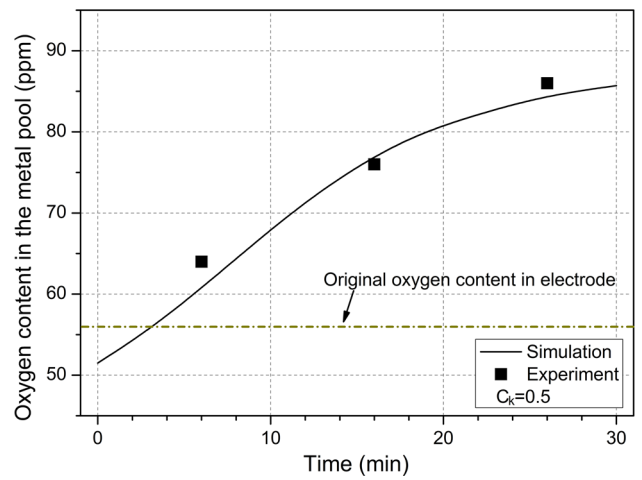


Fig. 8—Comparison of oxygen content in the metal pool between the simulation and experiment.

influence of gravity, surface tension, and electromagnetic force. In the present work, the alternative current flows in at the electrode tip, passes through the molten slag and liquid metal pool one by one as displayed in Figure 10. The current at the center of electrode tip tends to flow downward through the molten metal which has a lower electric resistance. According to Eq. [3], the Joule heating is closely related to the current density and electrical conductivity. Therefore, the Joule heating is mainly generated in the slag layer. The maximum value of the Joule heating can be observed near the slag around the droplet tip. Moreover, a higher region also locates at the slag beneath the periphery of the electrode tip because of the skin effect.

Figure 11 shows the flow field and temperature distribution at 1329.35 seconds. There are two apparent vortices in the longitudinal section of the slag layer as shown in Figure 11(a). The powerful shear stress provided by the periodically falling droplets dominates the vortex in the center of slag layer. The electromagnetic force around the droplet also contributes to it. Meanwhile, the strong cooling effect of the water-cooled mold drives the descending flow near the mold wall. The flow field is more complex in the liquid metal pool. Because the velocity magnitude in the slag layer is much larger than that in the liquid metal pool, the shear stress provided by the slag flow drives the liquid metal near the slag/metal pool interface, while the downward flow near the mold is attributed to the thermal buoyancy force. Although the Joule heating is the only heat source, the temperature distribution is slightly different from the Joule heating distribution due to the flow pattern. The hottest region locates under the periphery of electrode tip with a maximum value of 1986.2 K.

In this work, one of the most concerned issues is the thermodynamic relations at the interfaces among slag, metal, and air. The thermodynamic equilibrium constants are directly determined by the temperature distribution at the interfaces as shown in Figure 11(b). At the slag/metal droplet interface, the temperature decreases with height (mainly range from 1823.15 K to

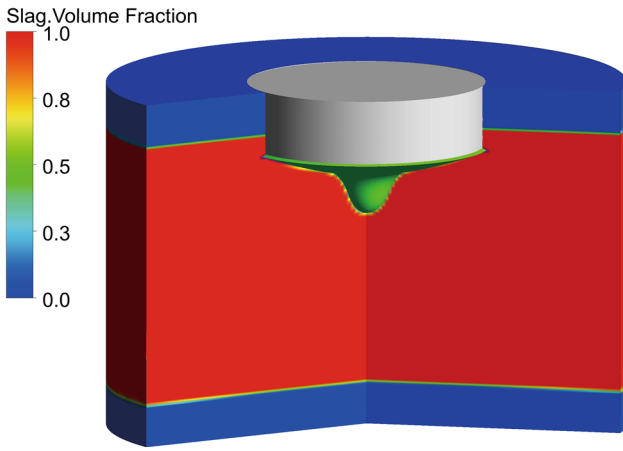


Fig. 9—Predicted distribution of slag phase at 1329.35 s.

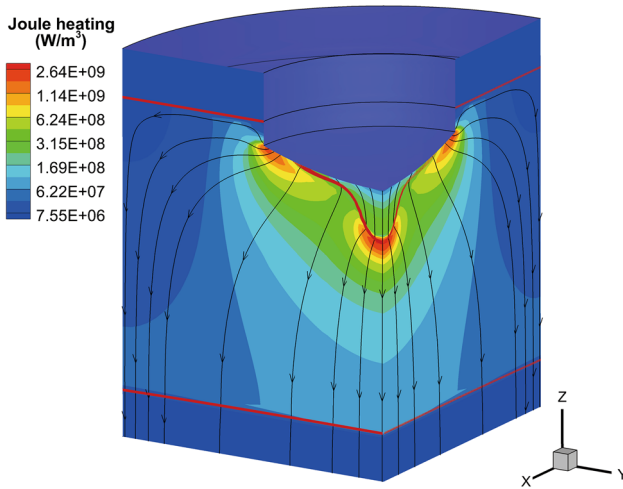


Fig. 10—Predicted distribution of current paths and Joule heating at 1329.35 s. The red line represents the interfaces among slag, metal, and air (Color figure online).

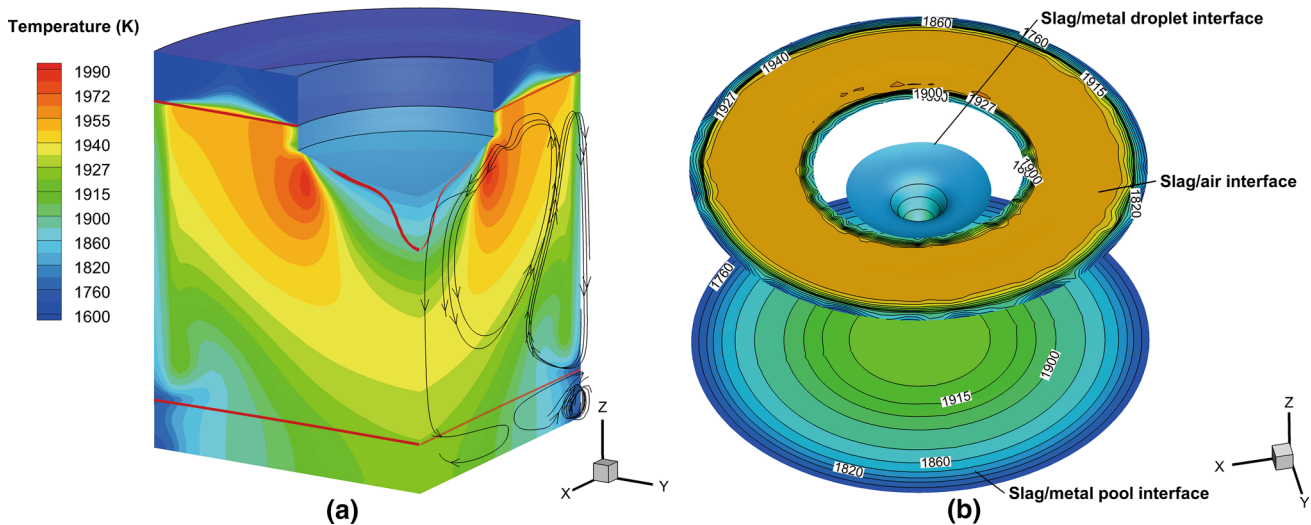


Fig. 11—Predicted temperature distribution and flow field at 1329.35 s: (a) Distribution of temperature and streamlines. (b) Temperature distribution at slag/metal and slag/air interfaces.

1900 K). At the slag/metal pool interface, there exists obvious radial temperature gradient (mainly range from 1760 K to 1925 K). The high temperature slag heats the falling droplets, and then results in a temperature rising in liquid metal pool. Therefore, a hotter region is observed in the center of the slag/metal pool interfaces, while a lower one near the mold owing to the cooling effect. Since the thermal conductivity of air is relatively small, a uniform temperature field (mainly range from 1860 K to 1940 K) can be seen at the slag/air interface. But the severe temperature gradient still remains near the mold and electrode.

C. Oxygen Transport Behavior

As described above, the mass transport process is based on the thermodynamics and the species concentrations in each phase. Therefore, the mass source terms of interfacial reactions $[\text{FeO}]-[\text{Fe}_2\text{O}_3]-[\text{Si}]-[\text{Mn}]-[\text{Al}]-[\text{O}]-[\text{O}_2]$ are calculated simultaneously by the kinetic model as shown in Figure 12. From Figure 12(a) we can see that the mass source term of oxygen is positive at the slag/metal droplet interface, which indicates that the oxygen will be absorbed into the metal phase. The mass source term close to the periphery of electrode and droplet tip is relatively higher due to the lower oxygen content in metal and the higher temperature, respectively. At the slag/metal pool interface, the source term is positive at the center and negative near the mold due to the temperature distribution. Particularly, the mass source term at the slag/metal droplet interface is about two orders of magnitude larger than that at the slag/metal pool interface because of the different specific surface areas for reactions. In Figure 12(b), the mass source term of FeO is positive at the slag/metal interface, which will cause an increase of FeO content in slag. According to Eq. [26], FeO is consumed at the slag/air interface with a uniform distribution of mass source term. In contrast, Fe_2O_3 , as an important carrier of oxygen from air to metal, is produced at the slag/air

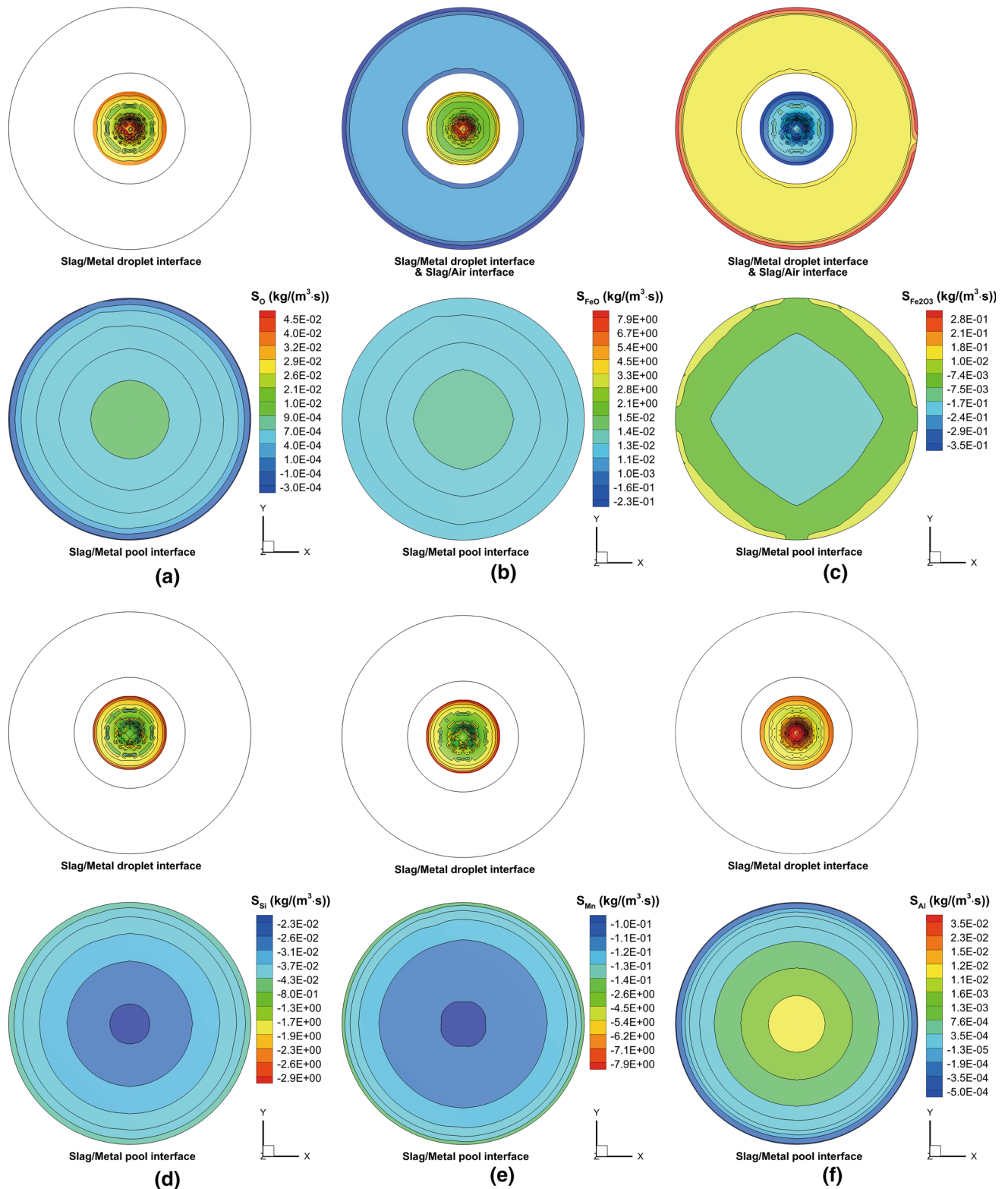


Fig. 12—Predicted distribution of mass source terms at the interfaces: (a) [O], (b) (FeO), (c) (Fe₂O₃), (d) [Si], (e) [Mn], and (f) [Al]. The interfaces shown in this paper are defined as the isosurfaces of 0.5 slag volume fraction.

interface and consumed at the slag/metal interface as displayed in Figure 12(c). As shown in Figures 12(d) and (e), the mass source terms of silicon and manganese are negative, which means these active elements are

oxidized by FeO. Due to the higher concentration of Al₂O₃ in slag, a small amount of aluminum is absorbed into the metal except the low temperature region as demonstrated in Figure 12(f). The dissolved aluminum

and oxygen will combine and form oxide inclusions during the solidification process, and finally influence the ingot quality.

In the present study, the oxide scale formed on the electrode during the ESR process is taken into account. The influence ratio, which is defined as the ratio of the mass source term of FeO caused by the scale oxide (Eq. [24]) to that by Fe_2O_3 (Eq. [19]), is illustrated in Figure 13. The influence ratio mainly ranges from 5 to 40, which indicates that the melt of the oxide scale is primarily responsible for the increase of FeO content in slag. This might be because the reaction $[\text{Fe}]-\{\text{O}_2\}$ at the metal/air interface is more efficient than Eq. [26] at the slag/air interface. It implies that some measures such as inert gas protection and anti-oxidation coating will significantly restrict the oxygen transport from air to metal.

Figure 14 shows the evolution of mass source term of species oxygen with time at the slag/metal droplet interface

interface. With the increase of FeO content from 12 to 28 minutes, the mass source term of species oxygen in metal gradually increases according to Eq. [15]. Hence, an increasing concentration of oxygen in the metal pool can be observed as described in Figure 8.

Figure 15 gives the evolution of the mass fraction of oxygen in metal within an averaged formation and falling period of metal droplet. This process lasts about 1.8 seconds, and the formation of metal droplet at the electrode takes up the most of the time. At the earlier stage, the oxygen content near the slag/metal droplet interface gradually increases due to the mass transfer process. The molten metal film with higher oxygen content is driven inward by the electromagnetic force and the gravity along the droplet surface as shown in Figure 15(a). With the growing of droplet, the formation starts to accelerate and an obvious concentration gradient can be observed in Figure 15(b). Subsequently, a slender neck is formed because of the high viscosity of metal as displayed in Figure 15(c). A similar phenomenon has been found in Kharicha's work.^[38] Meanwhile, the oxygen content gets homogeneous in the molten droplet. This concentration is slightly lower than that in the metal pool, which reflects that the mass transfer process in the metal pool cannot be ignored, although small. Since the slag layer thickness is relatively small, the molten droplet takes about 0.05 second detaching from the electrode and falling into the metal pool. The mass transport behavior is highly efficient in the slender neck owing to the more sufficient contact between slag and metal phases. As a result, the oxygen content increases rapidly in the slender neck as shown in Figure 15(d). Under the gravity and surface tension, the neck detaches from the electrode and forms another droplet as displayed in Figure 15(e). Finally, the rest of the neck breaks into small droplets as shown in Figure 15(f). During this process, the mass fraction of oxygen in the metal pool increases along radius direction due to the falling droplets. As discussed above, we can easily draw the conclusion that the oxygen transfer process is mainly achieved during the formation of the droplet at the slag/metal droplet interface.

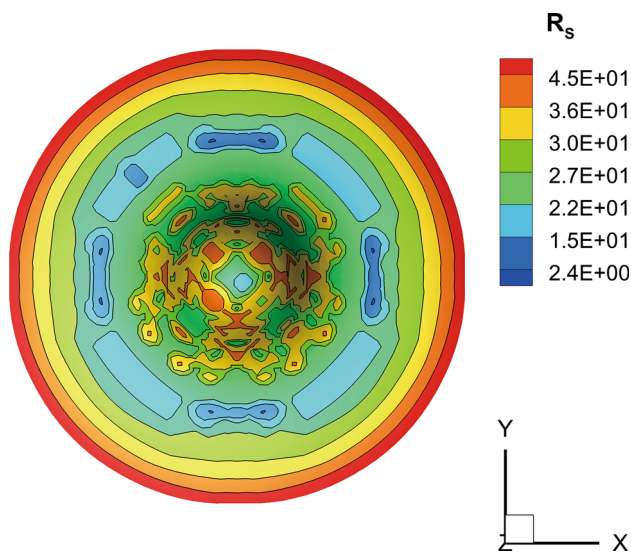


Fig. 13—Distribution of the influence ratio of mass source terms of FeO caused by Eq. [24] to that by Eq. [19].

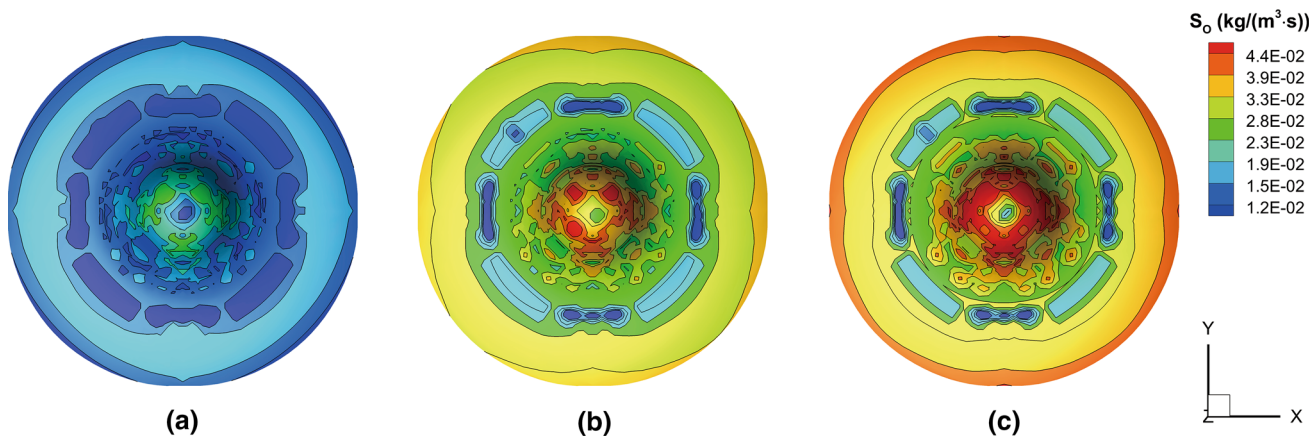


Fig. 14—Evolution of mass source term of species oxygen with time at the slag/metal droplet interface: (a) 12 min, (b) 20 min, and (c) 28 min.

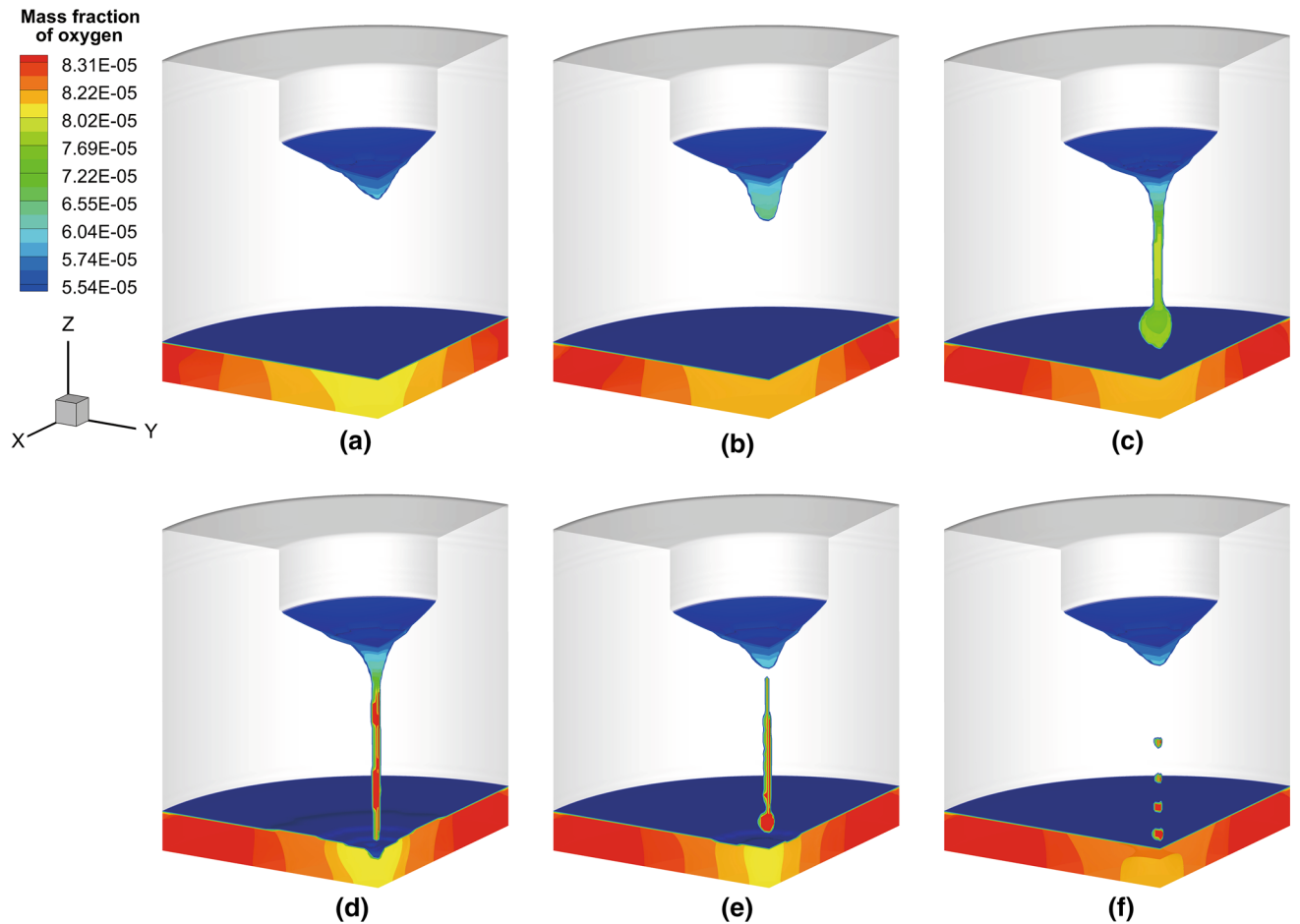


Fig. 15—Evolution of mass fraction of oxygen in metal with time: (a) 1328.40 s, (b) 1329.35 s, (c) 1329.70 s, (d) 1329.82 s, (e) 1329.90 s, and (f) 1330.18 s.

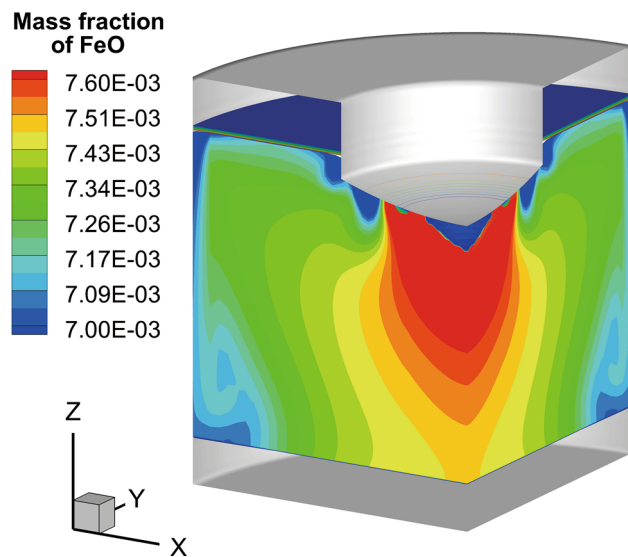


Fig. 16—Predicted distribution of mass fraction of FeO in slag at 1329.35 s.

Figure 16 illustrates the evolution of the FeO content distribution in slag at 1329.35 second. FeO represents the oxygen potential of slag in the present work, and is closely related with all the reactions. The higher concentration of FeO locates in the center of slag layer. This is because FeO is mainly produced at the slag/metal droplet interface, and is driven downward by the falling droplets. FeO is consumed at the slag/air interface, which results in a low concentration near the slag/air interface. Meanwhile, the flow pattern drives the slag with low FeO content inward near the electrode, or downward along the mold. Overall, the FeO content decreases along radius direction. Despite the FeO content increases as a function of time, it changes little in a short period.

D. The Effect of Current

Based on the foregoing discussions the effect of applied current on the oxygen transport behavior during ESR is investigated. The most immediate impact of current is the temperature distribution as shown in Figure 17. The increasing current creates more Joule

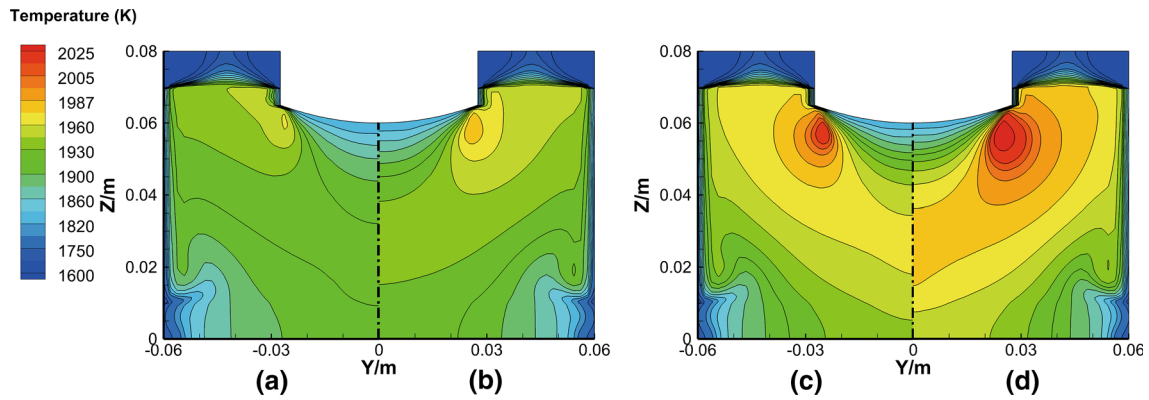


Fig. 17—Predicted temperature distribution with different currents: (a) 1200 A, (b) 1500 A, (c) 1800 A, and (d) 2100 A.

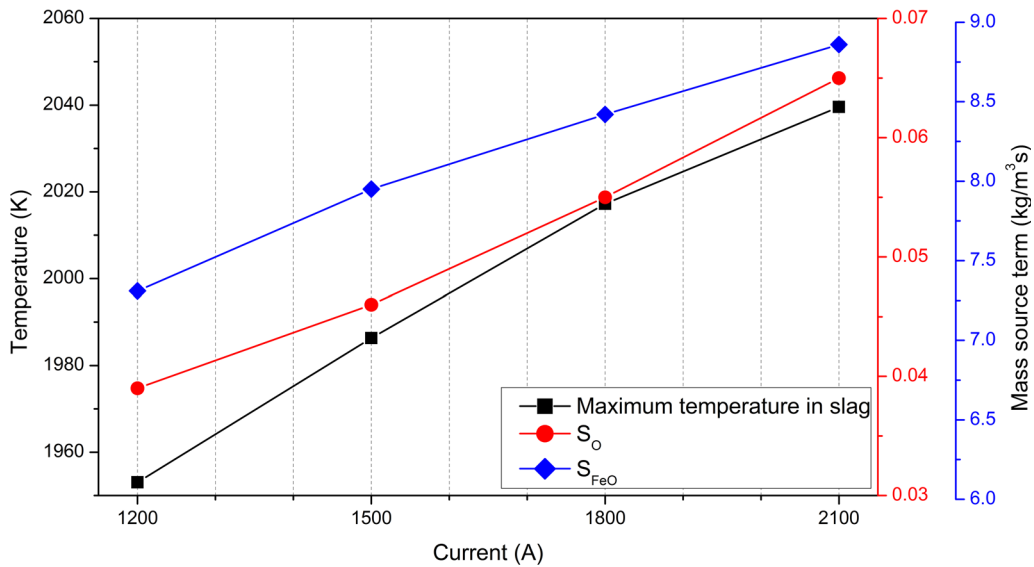


Fig. 18—Effect of current on slag temperature and mass source term.

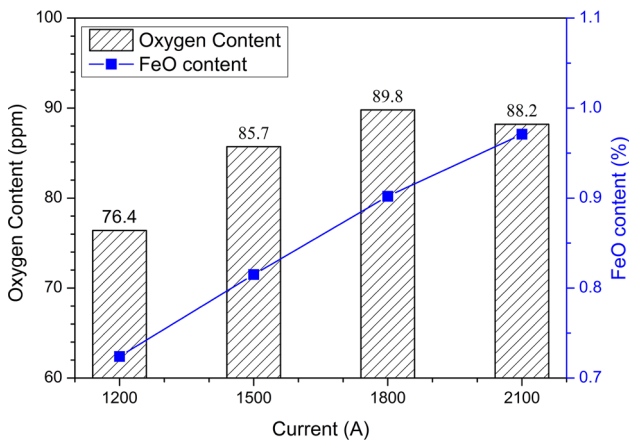


Fig. 19—Effect of current on oxygen content in the metal pool and FeO content in slag.

heating, and leads to a higher temperature distribution in turn. The high temperature is unfavorable for oxidation of silicon and manganese, and then the consumption of FeO decreases. The mass source term of FeO therefore increases with the applied current as shown in Figure 18. On the other hand, the high temperature will help oxygen move from the slag to metal according to Eq. [15]. Thus, the mass source term of oxygen also increases with the applied current.

Figure 19 displays the effect of current on the prediction of oxygen content in the metal pool and FeO content in slag. It can be found that the oxygen content and FeO content rise after the ESR process under the open atmosphere. With the current increasing from 1200 to 2100 A, the FeO content increases from 0.724 to 0.971 pct. This indicates that the applied current is proportional to the FeO content in slag. However, the oxygen content firstly increases from 76.4

ppm to 89.8 ppm with the current changes from 1200 to 1800 A, and then slightly declines to 88.2 ppm when the current increases to 2100 A. The maximum oxygen content is obtained when the current is 1800 A. This phenomenon might be the result of the competition between the increasing temperature and the decreasing total time of ESR process. Note that the higher current can also cause a deeper metal pool profile, which goes against the formation of columnar grain. Therefore, a lower applied current with an acceptable efficiency will be suggested to get the low oxygen content ESR ingot.

V. CONCLUSIONS

A transient 3D model has been developed to predict the oxygen transport behavior in ESR process. Using the coupled model, the electromagnetic field, heat transfer, three-phase flow, and species transport were solved simultaneously. Based on the necessary thermodynamics, a kinetic model was established to calculate the mass transfer process. The kinetic correction factor was proposed to account for the effect of the oxide scale on the FeO content in slag. Finally, the effect of applied current on the oxygen transfer behavior was studied. The simulated data agree well with the laboratory experiment with an acceptable discrepancy.

1. The powerful shear stress provided by the falling droplets as well as the electromagnetic force dominate the vortex in the center of slag layer, while the strong cooling effect drives the descending flow near the mold. The flow field makes the temperature distribution different from the Joule heating distribution, and the hottest region can be observed under the periphery of electrode tip.
2. The thermodynamics of oxygen transport behavior is determined by the temperature distribution at the interfaces. The mass source term in species transport equation of oxygen is positive at the slag/metal droplet interface, which reveals that the oxygen will be absorbed into the metal phase. FeO is consumed at the slag/air interface and produced at the slag/metal interface. The mass source term at the slag/metal droplet interface is about two orders of magnitude larger than that at the slag/metal pool interface.
3. The melt of the oxide scale formed on the electrode is proved to be the major reason of the increase of FeO content in slag. Some measures such as inert gas protection and anti-oxidation coating hence are considered to be the effective methods to prevent oxygen increasing in metal.
4. The oxygen transfer process is primarily achieved during the formation of the metal droplet at the slag/metal droplet interface. And the mass transfer process at the slag/metal pool interface could not be ignored, although small.
5. The higher current creating more Joule heating, and results in a hotter temperature distribution, affect the thermodynamics. With the current increasing from 1200 to 2100 A, the oxygen content in the metal first increases and then declines. The maximum oxygen

content, about 89.8 ppm, is obtained when the current is 1800 A.

ACKNOWLEDGMENTS

This work was supported by the National Natural Science Foundation of China (Grant Nos. U1508214 and 51574068).

NOMENCLATURE

a_i	Activity of species i
A	Specific surface area for reaction (1/m)
b	Inverse prandtl number
\vec{B}	Magnetic flux density (T)
c	Mass fraction of species i
C_k	Kinetic correction factor
c_p	Specific heat (J/(kg·K))
$\bar{D}_{eff,i}$	Effective diffusion coefficient of species i (m ² /s)
D_i	Diffusion coefficient of species i (m ² /s)
$D_{t,i}$	Turbulent diffusion coefficient of species i (m ² /s)
e_j^i	Interaction coefficient of the element j with respect to the element i
E	Internal energy of mixture phase (J/kg)
f_H	Electric current frequency (Hz)
f_i	Henry activity coefficient of species i
\vec{F}_e	Lorentz force (N/m ³)
\vec{F}_b	Buoyancy force (N/m ³)
\vec{F}_{st}	Surface tension (N/m ³)
\vec{g}	Gravity acceleration vector (m/s ²)
I_{RMS}	Root mean square current (A)
J	Current density (A/m ²)
k	Turbulent kinetic energy (m ² /s ²)
k_{eff}	Effective thermal conductivity (W/(m·K))
$k_{g,i} k_{m,i} k_{s,i}$	Mass transfer coefficient of species i in gas, metal, and slag (m/s)
$k_{T,i}$	Overall mass transfer coefficient of species i (m/s)
K	Reaction equilibrium constant
L	Latent heat of fusion (J/kg)
L_i	Interfacial distribution ratio of species i at equilibrium
\dot{m}	Melt rate (kg/s)
M_i	Molar mass of species i (kg/mol)
n	Normal vector
p	Pressure (Pa)
P_i	Partial pressure of species i (Pa)
Q_J	Joule heating (W/m ³)
r	Radius (m)
r_{max}	Inner radius of the mold (m)
R	Molar gas constant
R_S	Influence ratio
Sc_t	Turbulent schmidt number
S_i	Source term of species i in species transport equation (kg/(m ³ ·s))
t	Time (s)

T	Temperature (K)
\vec{v}	Velocity of mixture phase (m/s)
$w(i) w[i]$	Mass fraction of species i in slag and metal

GREEK SYMBOLS

α_i	Volume fraction of phase i
ϕ	Mixture phase property
μ_{0m}	Vacuum permittivity (F/m)
μ_{eff}	Effective viscosity (Pa·s)
μ_t	Turbulent viscosity (Pa·s)
σ	Electrical conductivity (1/(Ω ·m))
φ	Electrical potential (V)
ρ	Density (kg/m ³)
ρ_{em}	Electric resistance of metal (Ω ·m)
ε	Turbulent kinetic energy dissipation (m ² /s ³)
ν	Kinematic viscosity (m ² /s)
γ_i	Raoult activity coefficient of species i
δ	Electromagnetic skin depth (m)
η	Power efficiency coefficient

REFERENCES

1. A. Ludwig, A. Kharicha, and M. Wu: *Metall. Mater. Trans. B*, 2014, vol. 45B, pp. 36–43.
2. A. Kharicha, A. Mackenbrock, A. Ludwig, W. Schutzenhofer, V. Maronnier, M. Wu, O. Koser and R. Tanzer: *International Symposium on Liquid Metal Processing and Casting*, Nancy, 2007, pp. 107–113.
3. F. Reyes-Carmona and A. Mitchell: *ISIJ Int.*, 1992, vol. 32, pp. 529–37.
4. X.C. Chen, C.B. Shi, H.J. Guo, F. Wang, H. Ren, and D. Feng: *Metall. Mater. Trans. B*, 2012, vol. 43B, pp. 1596–1607.
5. A. Mitchell, F. Reyes-Carmona, and E. Samuelsson: *ISIJ Int.*, 1984, vol. 24, pp. 547–56.
6. D.G. Zhou, W.G. Xu, P. Wang, J. Fu, J.H. Xu, C.S. Wang, and D.M. Xu: *Iron Steel.*, 1998, vol. 33, pp. 13–17.
7. C.B. Shi, X.C. Chen, H.J. Guo, Z.J. Zhu, and H. Ren: *Steel Res. Int.*, 2012, vol. 83, pp. 472–86.
8. J.H. Wei and A. Mitchell: *Acta Metall. Sin.*, 1984, vol. 20, pp. 280–87.
9. V. Weber, A. Jardy, B. Dussoubs, D. Ablitzer, S. Ryberon, V. Schmitt, S. Hans, and H. Poisson: *Metall. Mater. Trans. B*, 2009, vol. 40B, pp. 271–80.
10. A. Kharicha, M. Wu, A. Ludwig, and E. Karimi-Sibaki: *Metall. Mater. Trans. B*, 2016, vol. 47B, pp. 1427–34.
11. Q. Wang, G.Q. Li, Z. He, and B.K. Li: *Appl. Therm. Eng.*, 2017, vol. 114, pp. 874–86.
12. Q. Wang, G.Q. Li, Y.M. Gao, Z. He, and B.K. Li: *J. Appl. Electrochem.*, 2017, vol. 47, pp. 445–56.
13. K. Fezi, J. Yanke, and M.J.M. Krane: *Metall. Mater. Trans. B*, 2015, vol. 46B, pp. 766–79.
14. J. Li, M. Wu, A. Ludwig, and A. Kharicha: *Int. J. Heat Mass Transf.*, 2014, vol. 72, pp. 668–79.
15. C.W. Hirt and B.D. Nichols: *J. Comput. Phys.*, 1981, vol. 39, pp. 201–25.
16. E. Karimi-Sibaki, A. Kharicha, J. Bohacek, M.H. Wu, and A. Ludwig: *Metall. Mater. Trans. B*, 2015, vol. 46B, pp. 2049–61.
17. A. Jardy, D. Ablitzer, and J.F. Wadier: *Metall. Mater. Trans. B*, 1991, vol. 22, pp. 111–20.
18. C. Byon: *Int. J. Heat Mass Transf.*, 2015, vol. 88, pp. 20–27.
19. P.G. Jonsson and L.T.I. Jonsson: *ISIJ Int.*, 2001, vol. 41, pp. 1289–1302.
20. C.P. Manning and R.J. Fruehan: *Metall. Mater. Trans. B*, 2013, vol. 44B, pp. 37–44.
21. M.E. Fraser and A. Mitchell: *Ironmak. Steelmak.*, 1976, pp. 279–87.
22. J.C. Lamont and D.S. Scott: *AICHE J.*, 1970, vol. 16, pp. 513–19.
23. W.T. Lou and M.Y. Zhu: *Metall. Mater. Trans. B*, 2014, vol. 45B, pp. 1706–22.
24. J.H. Wei and A. Mitchell: *Acta Metall. Sin.*, 1984, vol. 20, pp. 261–79.
25. S. Ban-Ya: *ISIJ Int.*, 1993, vol. 33, pp. 2–11.
26. A.J. Markworth: *Metall. Trans. A*, 1977, vol. 8, pp. 2014–15.
27. E. Shibata, H. Sun, and K. Mori: *Tetsu To Hagane*, 1999, vol. 85, pp. 27–33.
28. E. Karimi-Sibaki, A. Kharicha, J. Bohacek, M. Wu, and A. Ludwig: *Adv. Eng. Mater.*, 2016, vol. 18, pp. 224–30.
29. A. Kharicha, A. Ludwig, and M. Wu: *ISIJ Int.*, 2014, vol. 54, pp. 1621–28.
30. A. Mitchell: *Mater. Sci. Eng. A*, 2005, vol. 413, pp. 10–18.
31. F.P. Calderon, N. Sano, and Y. Matsushita: *Metall. Trans. B*, 1971, vol. 2B, pp. 3325–32.
32. M. Kawakami, S. Yokoyama, K. Takagi, M. Nishimura, and J.S. Kim: *ISIJ Int.*, 1997, vol. 33, pp. 425–31.
33. T. Emi and R.D. Pehlke: *Metall. Trans. B*, 1975, vol. 6B, pp. 95–101.
34. A.H. Dilawari and J. Szekeley: *Metall. Trans. B*, 1978, vol. 9B, pp. 77–87.
35. Q. Wang, Z. He, B.K. Li, and F. Tsukihashi: *Metall. Mater. Trans. B*, 2014, vol. 45B, pp. 2425–41.
36. Q. Wang, R.J. Zhao, M. Fafard, and B.K. Li: *Appl. Therm. Eng.*, 2015, vol. 80, pp. 178–86.
37. M. Choudhary and J. Szekeley: *Metall. Trans. B*, 1981, vol. 12B, pp. 418–21.
38. A. Kharicha, A. Ludwig and M. Wu: *International Symposium on Liquid Metal Processing and Casting*, Nancy, 2011, pp. 113–19.